RSC Advances

PAPER

Cite this: *RSC Adv.*, 2015, **5**, 16575

Enteromorpha based porous carbons activated by zinc chloride for supercapacitors with high capacity retention†

Mingbo Wu,* Peng Li, Yang Li, Jun Liu and Yang Wang

Porous carbons were prepared from enteromorpha overrunning in China Sea with $ZnCl_2$ as an active agent. The obtained porous carbons were used as electrode materials to make supercapacitors. In order to make enteromorpha based supercapacitors with high performance, the effects of preparation parameters, including impregnation weight ratio of $ZnCl_2$ to enteromorpha, activation time and temperature on pore structure and electrochemical performances of enteromorpha based porous carbons (EBPCs) were investigated. The specific area and porous structure were characterized by nitrogen adsorption. Galvanostatic charge–discharge and cyclic voltammetry analysis were used to investigate the electrochemical properties of EBPCs. The results show that activation temperature of 700 °C, the impregnation weight ratio of 2/1 and activation time of 1.5 h are the optimal preparation parameters. The prepared EBPC with a specific surface area of 1651 $m^2\ g^{-1}$ exhibited a specific capacitance of 206 F g^{-1} and capacity retention of 93% even after 5000 cycles, showing excellent electrochemical properties of EBPC and good future utilization of enteromorpha.

Received 29th October 2014
Accepted 22nd January 2015

DOI: 10.1039/c4ra13428a

www.rsc.org/advances

1. Introduction

Nowadays, the growing scarcity of fossil fuels and continually increasing greenhouse effect have impelled intensive research into creating environmentally effective energy storage devices all around the world. Among the energy storage devices, more and more attention has been paid to supercapacitors owing to their good electrochemical properties, *i.e.* high power density, high energy efficiency, excellent stability and long life cycle.[1–3] These advantages have promoted their applications in communication devices, portable devices, and electrical/hybrid vehicles. According to the energy storage mechanisms, there are mainly two types of supercapacitors, *i.e.* electric double layer capacitor (ions accumulate at the electrode/electrolyte interface) and pseudocapacitor (highly reversible redox reactions occur on the electrode).[4] Various materials, including porous carbon materials,[5] metal oxides[6,7] and conducting polymers,[8] have been used as electrodes of supercapacitors. Among these materials, porous carbons (PCs) with low cost, high specific surface area, environmentally friendly nature and relatively high conductivity,[9] have become the most popular materials for supercapacitors.

PC can be produced from various biomass precursors (*e.g.* wood,[10] fruit shells[11]) and some fossil-fuel based precursors, including petroleum[12] and coal. O. Terasaki *et al.* reported PC by pyrolyzing the furfuryl alcohol derived from subsidiary agricultural products within the pores of SBA-15.[13] Qiu *et al.* synthesized a new hierarchical PC from coal tar pitch with nano-Fe_2O_3 as the template and activation agent coupled with KOH activation.[5] Beyond the above mentioned raw materials, aquatic organism can also be used as PC precursors. F. Beguin *et al.* was reported to apply brown seaweed *Lessonia nigrescens* based PC obtained by one-step carbonization at 600 and 750 °C to supercapacitors in KOH media with a high capacitance of 188 F g^{-1} at a current density of 200 mA g^{-1}.[14] They also prepared carbon materials through direct pyrolyzation of sodium alginate, a widely-used biopolymer extracted from seaweed, at 600 °C under argon protection. The specific capacitance stabilize at 180 F g^{-1} after 6000 cycles in a two-electrode system.[15]

Enteromorpha is a type of marine macroalgae, as a result of eutrophication[16] it is harmful to ocean transportation, environment quality and tourism. During the last decade, enteromorpha green tides broke out annually in the Yellow Sea of China and devastated the coastal marine ecological systems.[17] Enteromorpha continues to thrive nowadays and the vast majority is sent to landfills or just decomposed on the sea beach, causing serious resource waste and environmental pollution. How to efficiently use enteromorpha has become a significant issue. For dried enteromorpha, the main components are moisture (10%), carbohydrate (48%), protein (21%), crude fibre (1.3%), fat (0.3%) and ash (18.6%),[18,19] most of which could serve as carbon precursors. Thus, we made an attempt to prepare PC from enteromorpha by $ZnCl_2$ activation. Compared

State Key Laboratory of Heavy Oil Processing, China University of Petroleum, Qingdao 266580, PR China. E-mail: wumb@upc.edu.cn; Tel: +86 532 8698 3452

† Electronic supplementary information (ESI) available. See DOI: 10.1039/c4ra13428a

with other active agents, such as H_3PO_4, KOH and K_2CO_3,[20,21] $ZnCl_2$ activation is milder and more controllable to obtain PC with higher surface area,[22] which is beneficial to the electrochemical performances. Thus, $ZnCl_2$ was selected as active agent in present work.

To the best of our knowledge, despite the growing interest in enteromorpha for bio-oil,[23] PC prepared from enteromorpha for supercapacitors has not been reported. Herein, the relationship between different process parameters and the electrochemical performances of EBPC as supercapacitor electrodes are reported.

2. Experimental

2.1. Preparation of EBPCs and their supercapacitors

Enteromorpha collected from Qingdao coastal district was washed with distilled water and dried thoroughly, then grinded into particles with size about 3 mm. After carbonized at 300 °C in a tubular furnace for 1.5 h, the as-prepared carbonized sample named pretreated enteromorpha (PE) was equally divided into three groups (I, II and III). All EBPCs were prepared under a nitrogen flow of 60 mL min^{-1} with a fixed heating rate of 5 °C min^{-1}. Group I was pyrolyzed at 600, 700 and 800 °C for 1.5 h and the resulting carbons were denoted as H600-0-1.5, H700-0-1.5 and H800-0-1.5, respectively. Group II was impregnated in 25 wt% $ZnCl_2$ (AR, Sinopharm Chemical Reagent Co., Ltd.) aqueous solution with mass ratios of $ZnCl_2$/PE at 1/1, 2/1 and 3/1, and dried overnight before activation at 700 °C for 1 h. The obtained samples were named H700-1-1, H700-2-1 and H700-3-1. Compared with group II, group III was impregnated in 25 wt% $ZnCl_2$ solution with a fixed mass ratio (2/1) and activated at 700 °C for 1.5 and 2 h. The carbons obtained were termed as H700-2-1.5, H700-2-2. The resulting samples of groups I, II and III were then washed 5 times with 5 M HCl and later washed with distilled water until a neutral pH was reached. The washed samples were dried at 100 °C overnight.

EBPCs were mixed with polytetrafluoroethylene (PTFE) binder and acetylene black as conductive additives in ethanol[24] with a mass ratio of 85 : 10 : 5. The electrode was obtained through coating the slurry onto a nickel foam with a diameter of 12 mm. Finally, the electrode was dried at 110 °C for 60 min in a vacuum oven. Two electrodes were separated by a polymer separator (Celgard 2400) in 6 M KOH solution before sandwiched in a CR2032 coin cell.

2.2. Sample characterization

The structures and morphologies of EBPCs were characterized by X-ray diffraction (XRD) (X'Pert PRO MPD, Holland) and field emission scanning electron microscopy (FE-SEM) (Hitachi S-4800, Japan). The functional groups in EBPCs were characterized by Fourier transform infrared spectrometry (FTIR) (Thermo Nicolet NEXUS 670, USA). X-ray photoelectron spectroscopy (XPS) was recorded on ESCALAB 250Xi spectrometer equipped with a pre-reduction chamber. The pore structure characterization was performed on the basis of low temperature nitrogen adsorption–desorption isotherms on a sorptometer (Micromeritics, ASAP 2020, America).

2.3. Electrochemical measurements

Galvanostatic charge–discharge (current load 50 to 1000 mA g^{-1}) and electrochemical impedance spectroscopy (EIS) with frequency ranging from 10 mHz to 100 kHz were used to investigate the electrochemical properties of EBPCs on a Land CT-2001A cell tester. The cyclic voltammetry (CV) analyses (scan rate 2 mV s^{-1}) were performed using a Princeton electrochemical workstation (PARSTAT 4000, Princeton, USA).

3. Results and discussion

XRD patterns of H700-2-1.5 and PE are shown in Fig. 1. For PE, XRD peaks at $2\theta = 16.2°$, 20.3°, 22.1°, 26.6°, 29.5°, 31.7°, 34.7°, 36.6° and 45.8° reveal the presence of silica (SiO_2, JCPDS#79-1906) and calcium sulfate ($CaSO_4$, JCPDS#73-1942). Despite these identified compounds, the unidentified peaks were probably attributed to trace metal compounds. After $ZnCl_2$ activation and acid washing, H700-2-1.5 had a broad peak at 15–35° corresponding to amorphous carbon, and the remaining peaks were attributed to silica, as shown in Fig. 1(b). The peaks of SiO_2 and amorphous carbon in H700-2-1.5 were apparently similar to those of H700-0-1.5 (see Fig. S1†), suggesting $ZnCl_2$ as active agent has not changed the basic crystallinity of the samples.

FTIR curves of PE and H700-2-1.5 are shown in Fig. 2. The weak bands at 3237 and 2924 cm^{-1} represent O–H vibration and C–H stretching, respectively, and the band at 1684 cm^{-1} was assigned to C=O stretching vibration. Peaks around 2375 cm^{-1} were caused by CO_2 molecule existed in air.[25] The C=C stretching vibration in aromatic rings of PE and H700-2-1.5 could also be identified by the peak around 1570 cm^{-1}, and the slender increase in peak intensity in H700-2-1.5 compared to PE attributed to the occurrence of condensation reaction during activation. FTIR curves also showed C–H deformation vibration at 1443 cm^{-1} while the strong transmission from 900 cm^{-1} to 600 cm^{-1} could be signed as fingerprint region of C–H on aromatic ring.[26,27] The weak peaks at 1104 cm^{-1} were assigned to C–O vibration.[28] There were fewer bands in the

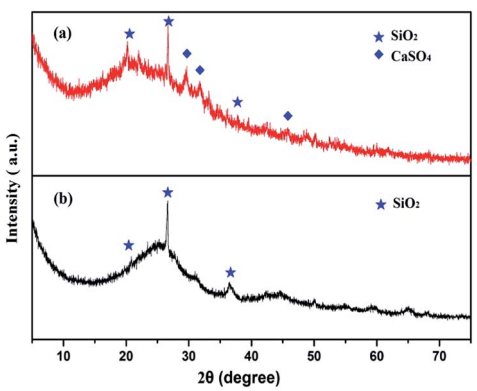

Fig. 1 XRD patterns of PE (a) and H700-2-1.5 (b).

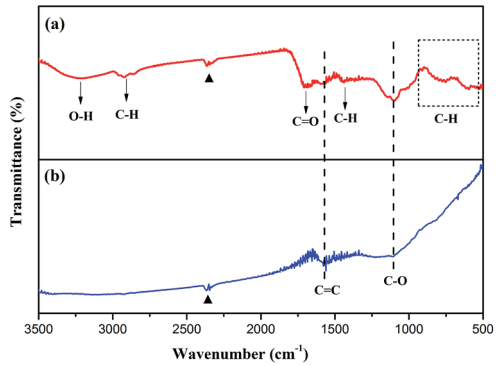

Fig. 2 FTIR spectra of PE (a) and H700-2-1.5 (b).

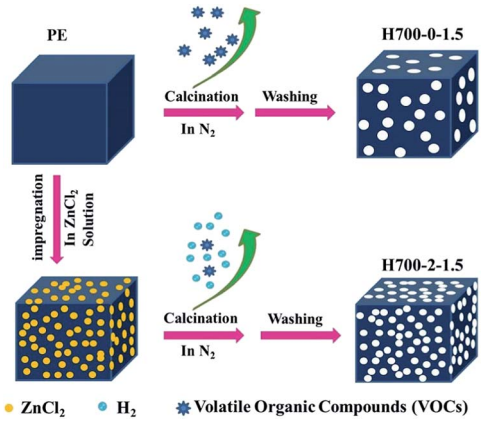

Fig. 4 Synthesis schematic of EBPC.

spectra of H700-0-1.5 (Fig. S2†) and H700-2-1.5 compared with that of PE owing to the high treatment temperature. In addition, the C=C bands of H700-0-1.5 were not as obvious as those of H700-2-1.5.

FE-SEM images in Fig. 3(a)–(c) show that PE, H700-0-1.5 and H700-2-1.5 have different morphologies. PE has smooth surface with little holes, H700-0-1.5 has some fractures and big holes as a result of high-temperature treatment while H700-2-1.5 has a rugged surface structure with many small pores after $ZnCl_2$ activation. PE, H700-0-1.5 and H700-2-1.5 can be imaged well without Au coating, suggesting that these samples possess good electrical conductivity. It can be deduced from the O 1s spectra of PE and H700-0-1.5 (see XPS spectra in Fig. 3(d)) that high temperature can give rise to oxygen loss due to the fracture of chemical bond involved in oxygen containing functional groups, which can also be seen from their FTIR curves in Fig. 2 and S2.† In comparison to H700-0-1.5, H700-2-1.5 had lower content of O and higher content of C (Fig. 3(d) and (e)). This change, as mentioned above, is most likely assigned to $ZnCl_2$ that leads to the charring and aromatization during the activation process.[29]

To clearly show the process of $ZnCl_2$ activation, a preparation mechanism for EBPC is proposed in Fig. 4. H700-0-1.5 was prepared through carbonization with volatile materials evolved from PE, resulting in a mass of pores, 53 v/v% of which were mesopores (see Table 1), while H700-2-1.5 with a micropore volume ratio of 93% was obtained by the activation of $ZnCl_2$ uniformly dispersed in PE. Under the promotion of $ZnCl_2$, the evolution of molecular hydrogen was more pronounced than other gaseous products.[21] H_2 gases were evolved from the hydroaromatic structure of the precursor and left some sites for reaction. Finally, removing the chemicals present in the carbonized sample *via* washing yielded porosity in the carbon structure.

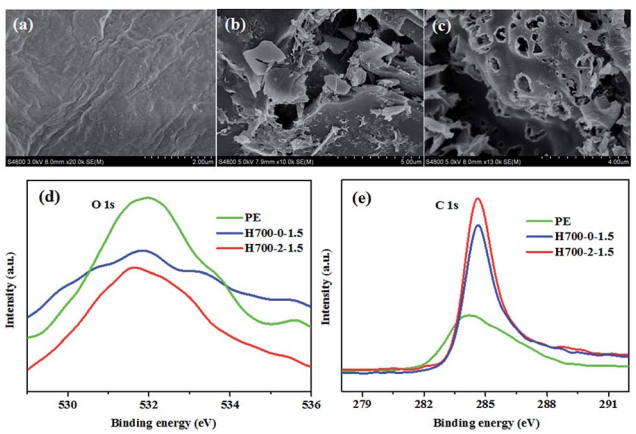

Fig. 3 SEM images of (a) PE, (b) H700-0-1.5 and (c) H700-2-1.5, XPS spectra of (d) O 1s and (e) C 1s of PE, H700-0-1.5 and H700-2-1.5.

3.1. The effect of temperature

Table 1 shows the effects of temperature, impregnation ratio ($ZnCl_2$/PE) and activation time on the yield and porous structure of obtained EBPCs. With the increasing temperature, porosity forms while yield descends along with the depolymerization of biomacromolecule (*e.g.* cellulose) and the generation of volatiles. For H700-0-1.5, due to the sufficient carbonization, the BET surface area (605 $m^2\ g^{-1}$) and total pore volume (0.48 $cm^3\ g^{-1}$) were much higher than those of H600-0-1.5 (131 $m^2\ g^{-1}$ and 0.17 $cm^3\ g^{-1}$).

However, as the temperature further increased to 800 °C, the surface area and pore volume decreased as a result of the partial extinction of micropores.[30]

Fig. 5 shows the N_2 adsorption–desorption isotherms of EBPCs. According to IUPAC classification method, adsorption–desorption isotherms of H600-0-1.5, H700-0-1.5 and H800-0-1.5 (Fig. 5(a)) belong to type IV isotherms and there are type H3 hysteresis loops, which is the most distinct characteristic of mesopores.[31] N_2 molecules were first adsorbed in micropores at low pressure stage as a result of strong interaction. Strong adsorption in mesopores and multilayer adsorption then begins to appear at medium pressure. Hysteresis loop is associated with capillary condensation.

Actually, the starting point of hysteresis loop corresponds to the appearance of capillary condensation. At high pressure, there is no limiting adsorption, indicating the existence of massive fracture pores due to the loose accumulation of flaky particles.[32] Fig. 6(a) shows the pore size distribution of H600-0-

Table 1 Pore structure and yield of EBPCs[a]

Sample	Yield (%)	BET surface area ($m^2\ g^{-1}$)	Total pore volume ($cm^3\ g^{-1}$)	Pore size (nm)	Micropore volume ($cm^3\ g^{-1}$)	V_{mi}/V_t (%)
H600-0-1.5	17	131	0.17	5.2	0.04	24
H700-0-1.5	15	605	0.48	3.2	0.24	47
H800-0-1.5	14	589	0.39	3.4	0.16	42
H700-1-1	19	1264	0.61	1.9	0.53	87
H700-2-1	23	1560	0.84	2.2	0.77	92
H700-3-1	24	1251	0.73	2.3	0.67	92
H700-2-1.5	21	1651	0.82	2.0	0.76	93
H700-2-2	20	1618	0.84	2.1	0.68	81

[a] V_{mi}: micropore volume; V_t: total pore volume.

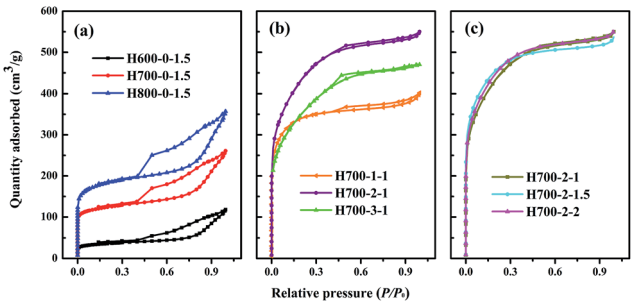

Fig. 5 Nitrogen adsorption–desorption isotherm curves of EBPCs.

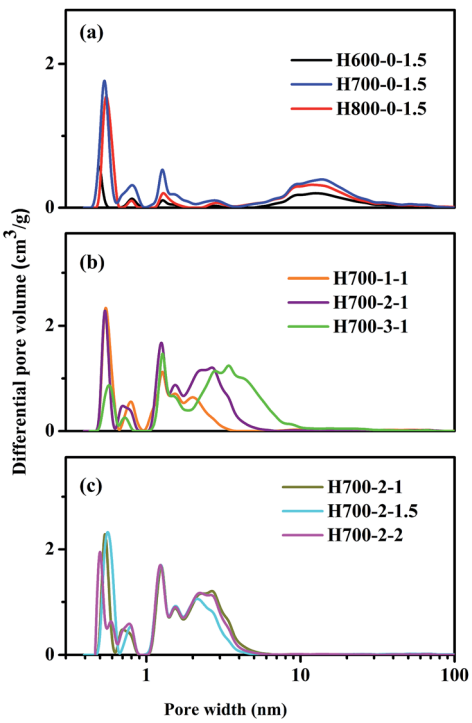

Fig. 6 Pore size distribution of EBPCs.

1.5, H700-0-1.5 and H800-0-1.5. Obviously, the pores of H600-0-1.5, H700-0-1.5 and H800-0-1.5 were mainly micropores and mesopores, which is consistent with Table 1.

Galvanostatic charge–discharge analysis carried out under different current densities is an effective method towards performance evaluation for supercapacitors. The electrode specific capacitance (C_p) is calculated by the following formula:

$$C_p = \frac{4I\Delta t}{m\Delta V} \quad (1)$$

where I (A), Δt (s), ΔV (V) and m (g) represent discharge current, discharge time, the potential drop in Δt and the mass of active material in two electrodes, respectively.

Fig. 7(a) shows the galvanostatic charge–discharge curves of EBPCs at the current density 100 mA g^{-1} in the voltage range 0–1 V. At different carbonization temperatures, the curves of H600-0-1.5, H700-0-1.5 and H800-0-1.5 exhibited high symmetry and linearity, indicating good supercapacitor behaviour. Moreover, the charge–discharge time of H700-0-1.5 and H800-0-

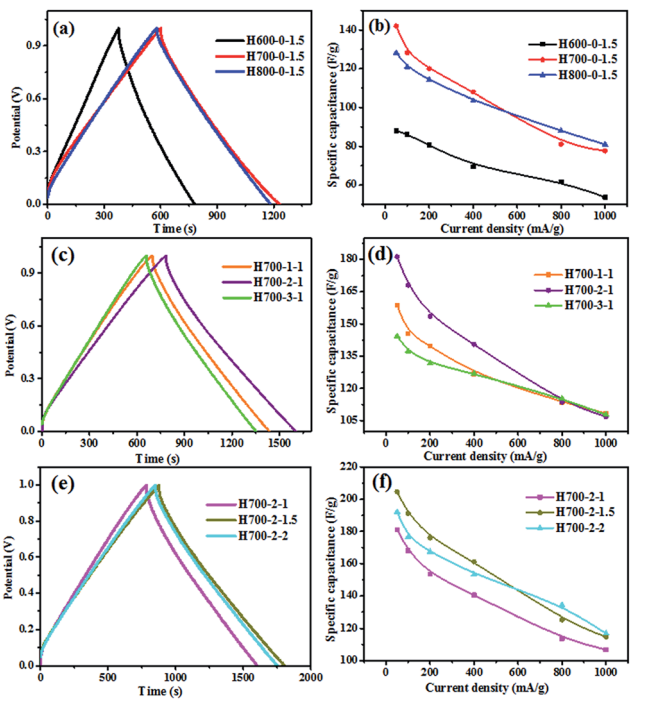

Fig. 7 Galvanostatic charge–discharge curves of EBPCs at 100 mA g^{-1} (a, c and e) and the specific capacitance of EBPCs at varied current densities (b, d and f).

1.5 were much longer than that of H600-0-1.5, indicating higher specific capacitance under the same current density. The varied specific capacitance at different current densities is shown in Fig. 7(b). When the current density was 50 mA g^{-1}, the specific capacitance of H700-0-1.5 was 144 F g^{-1}, which is much higher than 80 F g^{-1} of coconut shell, one of the most widely used biomass carbon materials.[33] The specific capacitance of H600-0-1.5, H700-0-1.5 and H800-0-1.5 retained 69, 108 and 103 F g^{-1} at 400 mA g^{-1}, demonstrating 700 °C the most favourable heating temperature for energy storage. However, H800-0-1.5 has a specific capacitance of 81 F g^{-1} at 1000 mA g^{-1}, relatively higher than 78 F g^{-1} of H700-0-1.5. The changes in the specific capacitance should be attributed to the different pore structures of EBPCs (Table 1). Cyclic voltammetry test was also used to further evaluate the electrochemical performance of H600-0-1.5, H700-0-1.5 and H800-0-1.5 (Fig. 8(a)). In ideal electric double layer capacitor electrolyte, ion migration should not be restricted and the cyclic voltammetry curve should be ideal rectangle under constant current and scan rate. The cyclic voltammetry curves of H600-0-1.5, H700-0-1.5 and H800-0-1.5 showed similar rectangles without apparent redox peaks, indicating that the pseudocapacitance contribution is little, and specific capacitance derives mainly from electric double layer capacitance.[34] In addition, the CV curve of H700-0-1.5 had a larger area than those of H800-0-1.5 and H600-0-1.5, indicating the highest specific capacitance, which can also be confirmed by galvanostatic charge–discharge curves in Fig. 7(a).

3.2. The effect of impregnation ratio

The impregnation ratio, namely the weight ratio of $ZnCl_2$/PE, is another crucial factor in $ZnCl_2$ activation process. The characteristics of EBPCs at 1 h of activation time and 700 °C of activation temperature with varied impregnation ratios of $ZnCl_2$/EP are listed in Table 1. As seen in Table 1, the yield, BET surface area and pore volume rose with increasing impregnation ratio from 1/1 to 2/1, which were attributed to the catalytic dehydroxylation and dehydration of $ZnCl_2$.[21] Volatiles, including formed hydrogen and oxygen, can promote the development of pores. As a type of Lewis acid, $ZnCl_2$ can promote the condensation of aromatic hydrocarbons. Nevertheless, at the ratio of 3/1, decreases were found both in BET surface area and the micropore volume due to the continuous enlargement of micropores.[35] H700-1-1 and H700-2-1 are microporous carbons evidenced by the type I isotherm in Fig. 5(b), while H700-3-1 have a certain amount of mesopores seen from its hysteresis loop, which can also be confirmed by the pore size distribution in Fig. 6(b).

Galvanostatic charge–discharge curves of H700-1-1, H700-2-1 and H700-3-1 are shown in Fig. 7(c). It can be easily seen that all the curves were relatively symmetrical and nearly linear with longer charge–discharge time than those of the unactivated samples (*i.e.*, H600-0-1.5, H700-0-1.5 and H800-0-1.5), showing higher specific capacitance. As shown in Fig. 7(d), the specific capacitances of H700-1-1, H700-2-1 and H700-3-1 were apparently higher than that of H700-0-1.5, reaching a maximum of 184 F g^{-1} (H700-2-1, 50 mA g^{-1}) followed by 160 F g^{-1} (H700-1-1). With the increase in current density, the capacitances of H700-1-1 and H700-2-1 decay fast as the ions in the electrolyte have difficulty in entering the pores in limited time. The attenuation of H700-3-1 was slow owing to its relatively higher mesopore ratios (Table 1). The electrochemical performances of H700-1-1, H700-2-1 and H700-3-1 were further evaluated by cyclic voltammetry curves in Fig. 8(b). Similar rectangles without apparent redox peaks reflect the typical characteristics of electric double layer supercapacitors. In addition, the CV curve area of H700-2-1 was larger than those of H700-1-1 and H700-3-1, indicating the highest specific capacitance and the most suitable impregnation ratio (2/1).

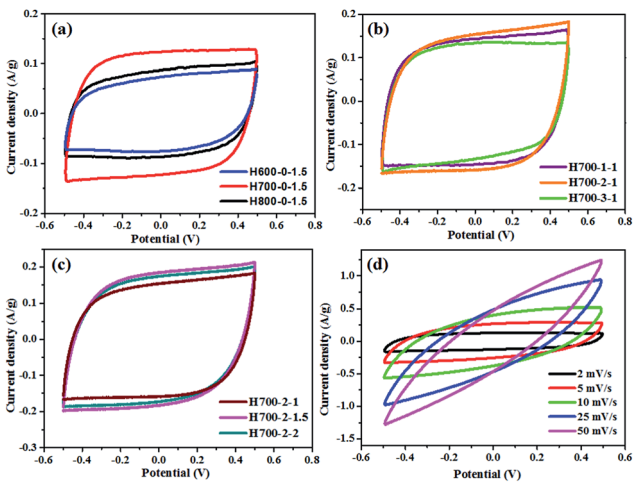

Fig. 8 CV curves of EBPCs at a scan rate of 2 mV s^{-1} (a–c) and CV curves of H700-2-1.5 at different scan rates (d).

3.3. The effect of activation time

Activation time is also an important influencing factor to the porous structure and electrochemical properties. With varied activation time (1, 1.5 and 2 h), the yield and pore structure parameters of EBPCs can be seen in Table 1. Notably, loss accretes in H700-2-1, H700-2-1.5 and H700-2-2 with the increase in activation time.

The N_2 adsorption–desorption curves of H700-2-1, H700-2-1.5 and H700-2-2 (apparently type I) are shown in Fig. 5(c). No hysteresis loops existed, suggesting that micropores account for the majority of pores, which is consistent with Fig. 6(c) and Table 1. Furthermore, the pore sizes of $ZnCl_2$ activated EBPCs were relatively smaller than that of unactivated samples (H600-0-1.5, H700-0-1.5 and H800-0-1.5). Junichi Hayashi[36] thinks that pneumatolytic $ZnCl_2$ plays a role of skeleton through dipping into the internal carbon, where the carbonized polymer deposits.

The effects of activation time on the electrochemical performance can be seen in Fig. 7(e) and (f), 8(c) and 9. Superior electrochemical properties can easily be seen from its high linearity and longer charge–discharge time in Fig. 7(e). When the current density was 50 mA g^{-1}, H700-2-1.5 has the largest specific capacitance (206 F g^{-1}), owing to the largest surface area (1651 m^2 g^{-1}) in Table 1. However, as the current density

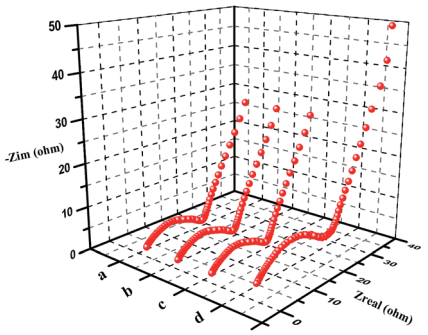

Fig. 9 EIS at (a) 0 V, (b) 0.5 V, (c) 1 V bias voltage of H700-2-1.5 and (d) EIS of H700-0-1.5.

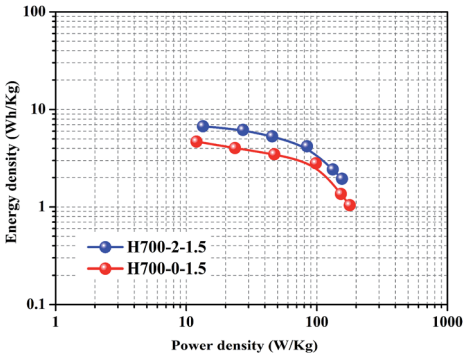

Fig. 11 Ragone plot of H700-2-1.5 and H700-0-1.5 supercapacitors.

increases from 50 mA g^{-1} to 1000 mA g^{-1}, the fastest decay occurred as a result of the minimal mesopore ratio. Furthermore, the nearly-rectangular CV curve of H700-2-1.5 has the largest area in Fig. 8(c), demonstrating the best electrical properties and the most suitable activation time, *i.e.* 1.5 h. Fig. 8(d) shows the cyclic voltammetry (CV) curves at various scan rates from 2 to 50 mV s^{-1}. As the scan rates increased, the CV curves became more and more oblique, an indicative of double layer capacitor behaviour.[37]

The Nyquist plots for the supercapacitors with H700-0-1.5 and H700-2-1.5 electrodes are shown in Fig. 9, and their electrical equivalent circuits are illustrated in Fig. S4.† Two electrodes have ideal electrochemical capacitance behaviour, *i.e.*, imaginary parts of impedance at low frequency region were nearly linear, which is typical of Warburg impedance, "*W*".[38] The plots also indicate that the supercapacitor with H700-2-1.5 electrodes had lower internal resistance (R_s) (1.41 Ω), seen from the point of intersecting with the real impedance (Z_{real}) axis in the range of high frequency.[37] In addition, smaller charge transfer resistance (R_{ct}) (14.38 Ω) of H700-2-1.5, which can be checked from the span of the single semicircle along the χ-axis from high to low frequency,[39] can obviously be seen compared with 22.09 Ω of H700-0-1.5. There is no doubt that $ZnCl_2$ activation enhanced the porosity, leading to the high specific capacitance and good electrochemical property for H700-2-1.5 electrode system. Furthermore, the EIS of H700-2-1.5 supercapacitor at different bias potentials from 0 to 1 V showed that there is no change with increasing bias potential, suggesting nonexistence of redox reaction or little effect of trace metal compounds on the electrochemical properties of EBPCs,[40] which has also been testified by CV test in Fig. 8(c).

Capacity retention rate is an important parameter for industrial application of the electrode material. The specific capacitances of H700-2-1, H700-2-1.5 and H700-2-2 electrodes before and after 5000 cycles at the same current density of 800 mA g^{-1} are shown in Fig. 10. All the electrodes have good cycle stability, and H700-2-1.5 had the highest specific capacitance both after 50 and 5000 cycles. The specific capacitance of H700-2-1, H700-2-1.5 and H700-2-2 electrodes, reached the highest value of 128, 136 and 129 F g^{-1} after 50 cycles at 800 mA g^{-1}, and 88% (113 F g^{-1}), 93% (126 F g^{-1}), 76% (99 F g^{-1}) can be retained even after 5000 cycles, indicating high capacity retention rate of EBPCs, especially for H700-2-1.5.

The Ragone plot (Fig. 11) shows the dependence between power density (P, W kg^{-1}) and energy density (E, W h kg^{-1}) of the supercapacitor with H700-2-1.5 electrodes, which are calculated in terms of the following equations:[41]

$$E = \frac{C_p \times \Delta V^2}{8} \times \frac{1000}{3600} \quad (2)$$

$$P = \frac{E}{\Delta t} \times 3600 \quad (3)$$

As can be seen in Fig. 11, H700-2-1.5 with zinc chloride activated had better electrochemical performances, which should be ascribed to higher specific area and better pore development.

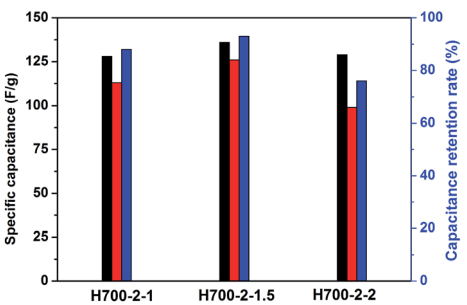

Fig. 10 The capacitance retention rate (blue) and the specific capacitance of H700-2-1, H700-2-1.5 and H700-2-2 after 50 (black), 5000 (red) cycles.

4. Conclusions

Marine pollutant (enteromorpha) was successfully used as the raw material to prepare porous carbon for the electrode material of supercapacitors. EBPCs obtained at the impregnation ratio ($ZnCl_2$/PE) of 2/1, activation time of 1.5 h and activation temperature of 700 °C has the best electrochemical properties with a specific capacitance of 206 F g^{-1} in 6 M KOH electrolyte at 50 mA g^{-1}. In addition, the obtained H700-2-1.5 had a capacity retention rate of 93% even after 5000 cycles, exhibiting high stability and promising electrochemical application of enteromorpha as electrode material for supercapacitors.

Acknowledgements

This work was supported by the National Natural Science Foundation of China (nos 51172285, 51372277); the Fundamental Research Funds for the Central Universities (14CX02060A).

References

1 J. R. Miller and P. Simon, *Science*, 2008, **321**, 651–652.
2 S.-H. Yu, X. Guo, D. Ling, D. Y. Chung, A. Jin, M. Shokouhimehr, T. Hyeon and Y.-E. Sung, *RSC Adv.*, 2014, **4**, 37365–37370.
3 Y. Wang, J. Xu, H. Wu, M. Xu, Z. Peng and G. Zheng, *J. Mater. Chem.*, 2012, **22**, 21923–21927.
4 G. Wang, L. Zhang and J. Zhang, *Chem. Soc. Rev.*, 2012, **41**, 797–828.
5 X. He, N. Zhao, J. Qiu, N. Xiao, M. Yu, C. Yu, X. Zhang and M. Zheng, *J. Mater. Chem. A*, 2013, **1**, 9440–9448.
6 X. Wang, A. Sumboja, M. Lin, J. Yan and P. S. Lee, *Nanoscale*, 2012, **4**, 7266–7272.
7 X. Lu, X. Huang, S. Xie, T. Zhai, C. Wang, P. Zhang, M. Yu, W. Li, C. Liang and Y. Tong, *J. Mater. Chem.*, 2012, **22**, 13357–13364.
8 R. Kötz and M. Carlen, *Electrochim. Acta*, 2000, **45**, 2483–2498.
9 L.-Z. Fan, Y.-S. Hu, J. Maier, P. Adelhelm, B. Smarsly and M. Antonietti, *Adv. Funct. Mater.*, 2007, **17**, 3083–3087.
10 M.-C. Liu, L.-B. Kong, P. Zhang, Y.-C. Luo and L. Kang, *Electrochim. Acta*, 2012, **60**, 443–448.
11 L. Sun, C. Tian, M. Li, X. Meng, L. Wang, R. Wang, J. Yin and H. Fu, *J. Mater. Chem. A*, 2013, **1**, 6462–6470.
12 M. B. Wu, Q. F. Zha, J. S. Qiu, X. Han, Y. S. Guo, Z. F. Li, A. J. Yuan and X. Sun, *Fuel*, 2005, **84**, 1992–1997.
13 K. Lund, N. Muroyama and O. Terasaki, *Microporous Mesoporous Mater.*, 2010, **128**, 71–77.
14 M. P. Bichat, E. Raymundo-Pinero and F. Beguin, *Carbon*, 2010, **48**, 4351–4361.
15 E. Raymundo-Pinero, F. Leroux and F. Beguin, *Adv. Mater.*, 2006, **18**, 1877–1882.
16 S. Zhao, B. Gao, X. Li and M. Dong, *Chem. Eng. J.*, 2012, **200–202**, 569–576.
17 W. Shi and M. Wang, *J. Geophys. Res.: Oceans*, 2009, 114.
18 M. Aguilera-Morales, M. Casas-Valdez, S. Carrillo-Domínguez, B. González-Acosta and F. Pérez-Gil, *J. Food Compos. Anal.*, 2005, **18**, 79–88.
19 B. S. Mamatha, K. K. Namitha, A. Senthil, J. Smitha and G. A. Ravishankar, *Food Chem.*, 2007, **101**, 1707–1713.
20 J. Hayashi, T. Horikawa, I. Takeda, K. Muroyama and F. N. Ani, *Carbon*, 2002, **40**, 2381–2386.
21 A. Ahmadpour and D. D. Do, *Carbon*, 1997, **35**, 1723–1732.
22 D. Kalderis, S. Bethanis, P. Paraskeva and E. Diamadopoulos, *Bioresour. Technol.*, 2008, **99**, 6809–6816.
23 J. Li, G. Wang, Z. Wang, L. Zhang, C. Wang and Z. Yang, *J. Anal. Appl. Pyrolysis*, 2013, **104**, 494–501.
24 L. Bonnefoi, P. Simon, J. F. Fauvarque, C. Sarrazin, J. F. Sarrau and A. Dugast, *J. Power Sources*, 1999, **80**, 149–155.
25 M.-H. Wang, Z.-Y. Zhao and T.-T. Liu, *J. Alloys Compd.*, 2015, **621**, 220–224.
26 R. Bissessur, P. K. Y. Liu, W. White and S. F. Scully, *Langmuir*, 2006, **22**, 1729–1734.
27 J. W. Peckett, P. Trens, R. D. Gougeon, A. Pöppl, R. K. Harris and M. J. Hudson, *Carbon*, 2000, **38**, 345–353.
28 X. Liu, X. Qi, Z. Zhang, L. Ren, G. Hao, Y. Liu, Y. Wang, K. Huang, X. Wei, J. Li, Z. Huang and J. Zhong, *RSC Adv.*, 2014, **4**, 13673–13679.
29 X. He, P. Ling, M. Yu, X. Wang, X. Zhang and M. Zheng, *Electrochim. Acta*, 2013, **105**, 635–641.
30 A. Gurses, C. Dogar, S. Karaca, M. Acikyildiz and R. Bayrak, *J. Hazard. Mater.*, 2006, **131**, 254–259.
31 G.-R. Li, Z.-P. Feng, Y.-N. Ou, D. Wu, R. Fu and Y.-X. Tong, *Langmuir*, 2010, **26**, 2209–2213.
32 K. S. W. Sing, D. H. Everett, R. A. W. Haul, L. Moscou, R. A. Pierotti, J. Rouquerol and T. Siemieniewska, in *Handbook of Heterogeneous Catalysis*, Wiley-VCH Verlag GmbH & Co. KGaA, 2008.
33 P.-w. Zhou, B.-h. Li, F.-y. Kang and Y.-q. Zeng, *New Carbon Mater.*, 2006, **21**, 125–131.
34 M. Biswal, A. Banerjee, M. Deo and S. Ogale, *Energy Environ. Sci.*, 2013, **6**, 1249–1259.
35 N. R. Khalili, M. Campbell, G. Sandi and J. Golaś, *Carbon*, 2000, **38**, 1905–1915.
36 J. i. Hayashi, A. Kazehaya, K. Muroyama and A. P. Watkinson, *Carbon*, 2000, **38**, 1873–1878.
37 Z. Zhang, X. Liu, X. Qi, Z. Huang, L. Ren and J. Zhong, *RSC Adv.*, 2014, **4**, 37278–37283.
38 J. Wang, Y. Xu, F. Yan, J. Zhu and J. Wang, *J. Power Sources*, 2011, **196**, 2373–2379.
39 X. Liu, X. Qi, Z. Zhang, L. Ren, Y. Liu, L. Meng, K. Huang and J. Zhong, *Ceram. Int.*, 2014, **40**, 8189–8193.
40 E. Frackowiak, K. Metenier, V. Bertagna and F. Beguin, *Appl. Phys. Lett.*, 2000, **77**, 2421–2423.
41 H. Yu, J. Wu, L. Fan, Y. Lin, K. Xu, Z. Tang, C. Cheng, S. Tang, J. Lin, M. Huang and Z. Lan, *J. Power Sources*, 2012, **198**, 402–407.